

# Friction compensation for an m-Level telescope based on high-precision LuGre parameters identification

Yan-Rui Su (苏艳蕊)<sup>1,2</sup>, Qiang Wang (王强)<sup>3</sup>, Fa-Bao Yan (严发宝)<sup>1,2,4</sup> and Yong-Mei Huang (黄永梅)<sup>3</sup>

<sup>1</sup> School of Mechanical, Electrical & Information Engineering, Shandong University, Weihai 264209, China

<sup>2</sup> Laboratory for Electromagnetic Detection, Institute of Space Sciences, Shandong University, Weihai 264209, China; [hjc-8555@sdu.edu.cn](mailto:hjc-8555@sdu.edu.cn)

<sup>3</sup> Institute of Optics and Electronics, Chinese Academy of Sciences, Chengdu 610209, China

<sup>4</sup> CAS Key Laboratory of Solar Activity, National Astronomical Observatories, Chinese Academy of Sciences, Beijing 100101, China

Received 2020 April 30; accepted 2020 July 2

**Abstract** Friction torque severely weakens the tracking accuracy and low-speed stability of an m-level TCS (telescope control system). To solve this problem, a friction compensation method is proposed, based on high-precision LuGre friction model parameters identification. Together with dynamometer calibration, we first design a DOB (disturbance observer) to acquire high-accuracy TCS friction value in real time. Then, the PSO-GA (a hybrid algorithm combined particle swarm optimization algorithm and genetic algorithm) optimization algorithm proposed effectively and efficiently realizes the LuGre model parameters identification. In addition, we design a TCS controller including DOB and LuGre model parameters identification based on double-loop PID controller for practical application. Engineering verification tests indicate that the accuracy of DOB calibrated can reach 96.94% of the real measured friction. When azimuth axis operates in the speed cross-zero work mode, the average positive peak to tracking error reduces from 0.8926'' to 0.2252'' and the absolute average negative peak to tracking error reduces from 0.8881'' to 0.3984''. Moreover, the azimuth axis tracking MSE reduces from 0.1155'' to 0.0737'', which decreases by 36.2%. Experimental results validate the high precision, facile portability and high real-time ability of our approach.

**Key words:** telescopes — instrumentation: detectors — methods: analytical

## 1 INTRODUCTION

When m-level aperture optoelectronic telescopes operate in low-speed or speed cross-zero modes, their large rotational inertia brings the problem that the friction influence increases and the jitter phenomenon appears (Li et al. 2019; Wang et al. 2019; Su et al. 2016). The influence of friction on TCS can be summarized as Table 1.

The impact factors of TCS friction are complex, and include rotational velocity, rotational position, turntable

material, turntable weight, internal friction of the actuator, temperature and lubricant type. (Gajewski & Glogowski 2015). To weaken the friction influence on a control system's ATP (aiming, tracking and positioning) accuracy and running stability, the research on friction compensation technology is ongoing (Tang et al. 2017).

To achieve accurate friction values, transfer method of parameter variation (Jorge et al. 2018), power transformation method (Xie 2010) and balancing moment method (Wu et al. 2017) are three commonly used approaches. However, the measurement of motor friction torque generally separates from its application turntable and friction torque values measured or provided are without dynamic characteristics at present.

As for friction compensation technologies, there are two kinds: the non-model-based method (Goubej et al.

**Table 1** The Influence of Friction on TCS Performance

No	TCS task	Friction influence
1	Aiming and positioning	Steady-state error
2	Reversing tracking	Tracking discontinuity
3	One-way low-speed tracking	Creeping phenomenon
4	High-speed operation	Tracking error

2017; Rafan et al. 2016) and the model-based method (Qin et al. 2016).

Non-model-based friction compensation methods are studied continuously. A neural network-based approach to friction compensation is proposed for robot control in (Guo et al. 2019). A synchronization controller is designed for the dynamic friction compensation in a networked Lagrange system in Jiang et al. (2018). A control strategy for the active compensation of friction in a column-assist-type EPS is presented (Wilhelm et al. 2016). A discrete-time direct model reference adaptive control based on nonlinear friction compensation is introduced to a PI system in (Ke et al. 2019). A controller with feedback PI control and a pre-filter for dynamic compensation is proposed in (Lopes et al. 2019). An adaptive integral backstepping sliding mode control approach with friction compensation is developed for a fast moving target in (Yue et al. 2017). A cascade acceleration feedback control (AFC) enhanced by a disturbance observation and compensation (DOC) method to suppress friction is proposed in Wang et al. (2016). To overcome the negative effect of wind and friction on the Large Sky Area Multi-Object Fiber Spectroscopic Telescope (LAMOST), a third order Higher Order Sliding Mode (HOSM) controller is demonstrated in Zhou et al. (2010).

Non-model-based friction torque compensation technologies suppress the total interference, not only the friction, which is not conducive to the specific analysis of friction disturbance rejection. For model-based friction compensation technologies, dynamic friction models are mainstream models, which mainly include the Dahl model (Dahl 1976), the reset integrator model (Haessig & Friedland 1991), the Bliman-Sorine model (Brokate 2000), and the LuGre model (Canudas de Wit et al. 1995), etc. The existence of the Stribeck effect ensures that no model can give a completely and accurately mathematical description for friction yet (Wilhelm et al. 2016).

Through comparison, we choose LuGre model as TCS friction model, which describes friction mathematical continuously to ensure friction transit from stage to stage smoothly and easy implementation. The method that combined with nonlinear curve fitting techniques and second order LTI system is proposed to identify the LuGre model to compensate for the friction in one Schmidt telescope's R.A. axis based on a PI controller in Kumar & Banavar (2011). A research, which modified LuGre model through adjusting its parameters for servomechanism friction compensation is investigated in Sun et al. (2018). A modified LuGre model represented by a pair of masses separated by a linear spring for the velocity reversal system of an astronomical telescope

is proposed in Kumar & Banavar (2018). An approach based on a great many different conditional experiments for LuGre model parameters identification is presented in Puglisi et al. (2017). An adaptive friction compensation method based on the LuGre model for robust with cascaded structure is given in Le-Tien & Albu-Schaffer (2018). Physical motivation with parametric description to modify LuGre model is proposed in Iskandar & Wolf (2019).

However, there are some deficiencies of existing friction compensation methods based on LuGre model. The parameter identification accuracy is not high enough for TCS precision to reach up to arcsecond level. Special motion state requests in parameters identification process are needed. In addition, overly-complicated friction compensation methods may weaken TCS real-time quality and hurt TCS stability.

In this study, we proposed a friction compensation method combined with DOB friction measurement and LuGre parameters identification based on a PSO-GA algorithm. In addition, its corresponding controller is designed to realize high-accuracy real-time friction compensation. The effectiveness of the proposed method is verified by engineering practice.

## 2 HIGH-ACCURACY FRICTION TORQUE MEASUREMENT

To establish TCS LuGre friction model, it is essential to obtain accurate and continuous friction torque of TCS axes first, as shown in Figure 1.

### 2.1 Torque Sensor Technology

The most direct way for friction measurement is to install torque sensor on TCS servo turntable. Figure 2 displays a servo system with torque measurement. The torque sensor is installed between the motor and load by means of rigid or flexible coupling.

The torque sensor can measure the friction torque directly. When friction affects the turntable, electronic sensor receives the disturbance, and its output voltage or current changes correspondingly, which is then converted into the digital signal input of the controller to affect system operation. Similarly, the friction torque can be compensated directly in TCS.

This method does not rely on disturbance model, and can offset the nonlinear disturbance impact on TCS tracking precision and speed stability directly. Compared with other torque measurement methods, it is the most accurate method of measurement (Chen et al. 2012).

However, for TCS, the torque sensors are large and expensive. The installation of torque measuring devices

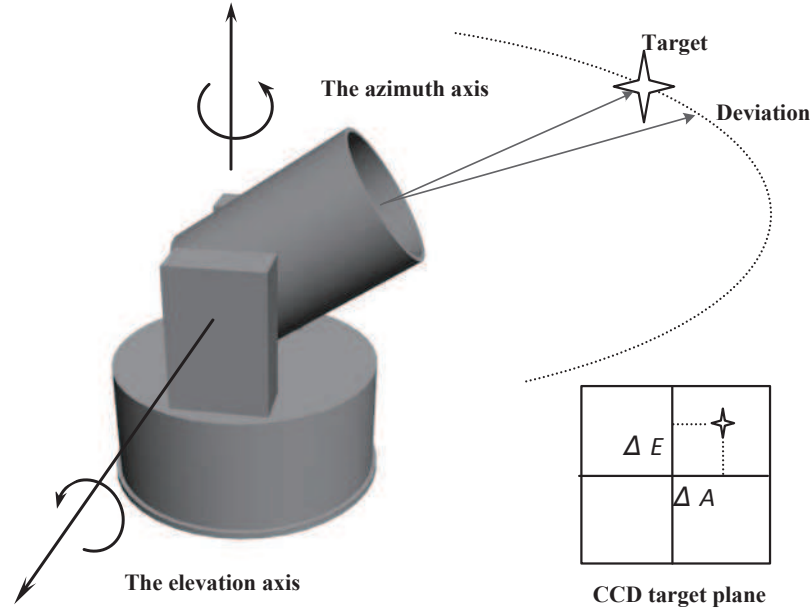


Fig. 1 TCS axes in ATP: azimuth axis and elevation axis.

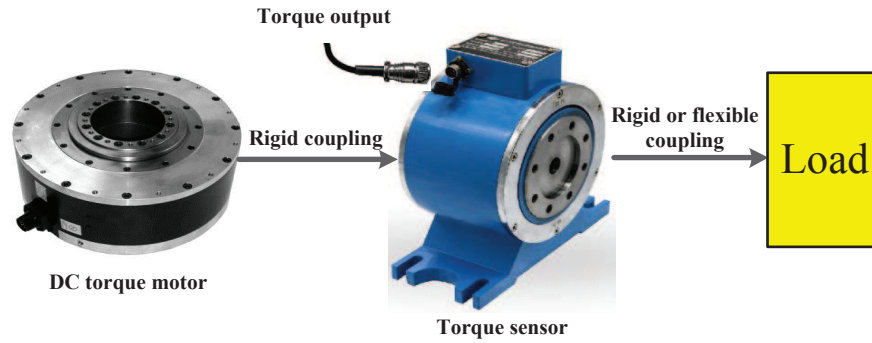


Fig. 2 Traditional torque measurement method using a torque sensor.

increases TCS flexibility, accompanied with the reduction of TCS stiffness and robustness.

## 2.2 High-precision Friction Acquisition Based on Torque Sensor and DOB Technology

DOB has advantages in compensating for estimated disturbance in real time. However, it brings with a distinct drawback in that DOB is vulnerable to the interference, particularly the internal parameter variation of the control system.

To draw on each other's merits of torque sensor method and DOB technique, DOB is selected to realize real-time torque measurement and a portable pull-push dynamometer is chosen as TCS friction torque sensor to calibrate DOB. The portable digital display pull-push dynamometer is with the feature of high precision, low cost and small size.

The DOB for TCS friction acquisition is designed as shown in Figure 3 for the speed loop of TCS.

An estimate of friction torque  $\hat{T}_d(s)$  can be expressed via Equation (1).

$$\hat{T}_d(s) = \dot{\theta}(s)G_n(s)^{-1} - u(s) \quad (1)$$

where  $\hat{T}_d(s)$  represents the friction observed,  $\dot{\theta}(s)$  denotes the speed of TCS axes,  $G_n(s)$  is the nominal model of the controlled plant  $G_p(s)$ , and  $u(s)$  is the output of the speed loop controller  $C_v$  and the input of DOB.

The torque measurement of TCS azimuth axis by dynamometer is shown as Figure 4. The push-pull type dynamometer is fixed in azimuth servo turntable tangentially and communicates with computer via a serial cable. Then computer serial interface reads the friction torque measured in real time.

According the principle of equilibrium in mechanics, when TCS states in uniform motion, thrust force equals to the friction. The state of the TCS can be read

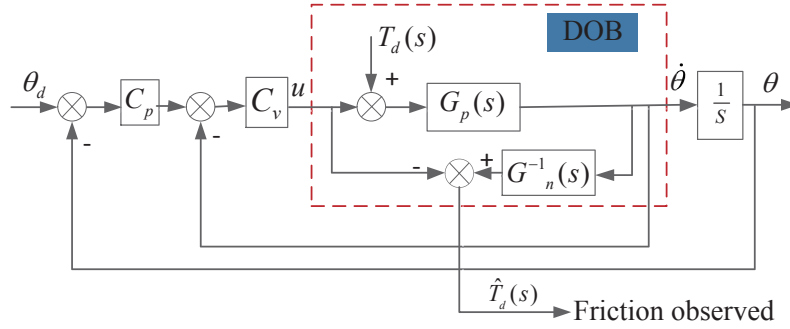


Fig. 3 TCS Friction torque observation.

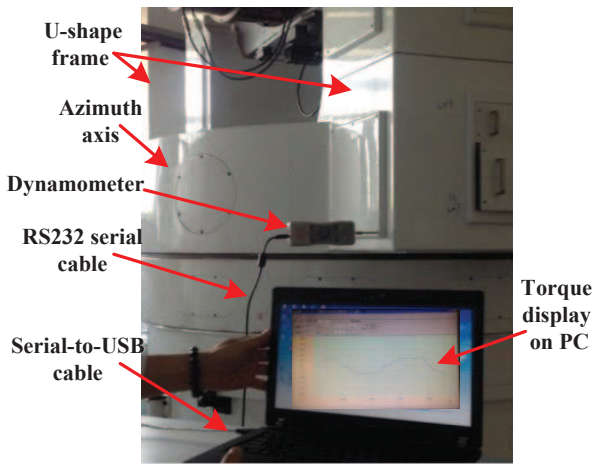


Fig. 4 Digital-display dynamometer measuring TCS azimuth axis friction torque.

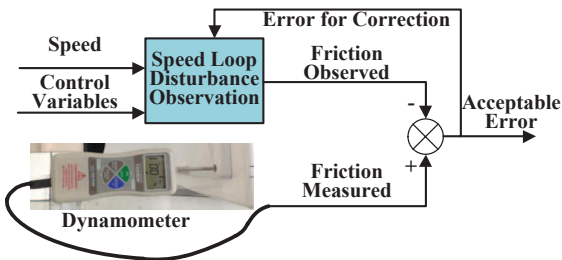


Fig. 5 Dynamometer calibrates the friction observed by DOB.

through inertial data achieved by steel scale tape angle encoder, which is produced by HEIDENHAIN with a precision of  $\pm 3\mu\text{m}$ . The thrust force value can be achieved by dynamometer data directly through serial port. The dynamometer has an accuracy of 0.1% *F.S.* The dynamometer is installed in the tangential direction of the azimuth axis turntable with the help of electric inclinometer.

High-precision friction acquirement based on torque sensor and DOB Technology is designed, which DOB works cooperatively with dynamometer (see Fig. 5).

By simultaneous dynamometer correction, DOB parameters reach optimal values within an allowable range of error. Then the friction observed and friction measured are considered equal. The dynamometer will be removed after the DOB calibration.

For this approach to obtaining friction, engineers need not install torque sensor mechanically on TCS and can acquire high-accuracy friction by DOB in real time as well. This method is to acquire an accurate, continuous and real-time friction measurement.

### 3 LUGRE MODEL PARAMETERS IDENTIFICATION

By means of a comparative analysis of existing friction models, LuGre model can describe probably the most important friction inner dynamic properties, such as stick-slip, pre-sliding displacement, static friction force variability, friction lag, Stribeck effect, etc. In addition, LuGre model provides a continuously mathematical friction description to ensure a smooth transition from friction stage to stage, which makes easy engineering implementation. The LuGre model is chosen as the TCS friction model.

#### 3.1 LuGre Friction Model

LuGre model is based on Dahl model and microscopic surface bristles hypothesis, as shown in Figure 6 (Canudas de Wit et al. 1995).

The LuGre model mathematical expression is as follows.

$$\frac{dz}{dt} = \omega - \frac{|\omega|}{g(\omega)}z \quad (2)$$

$$g(\omega) = M_c + (M_S - M_c)e^{-\left(\frac{\omega}{\omega_S}\right)^2} \quad (3)$$

$$M_f = \sigma_0 + \sigma_1 \frac{dz}{dt} + \sigma_2 \omega \quad (4)$$

where  $z$  denotes the average deflection of bristles, which can be acquired by torque observer.  $M_c(N)$  is the Coulomb friction,  $M_S(N)$  is the maximum static friction

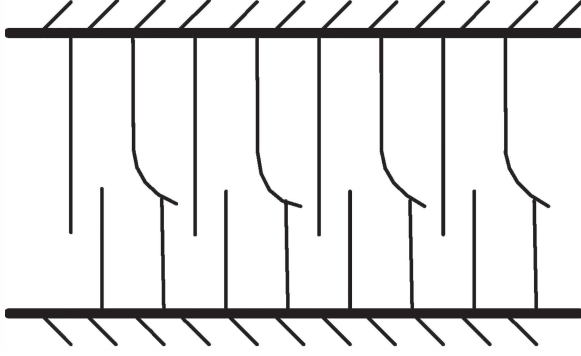


**Fig. 6** Bristle friction model.

force, and  $\omega_S$  ( $^\circ/s$ ) is the Stribeck velocity,  $\sigma_0$  ( $N\ m^{-1}$ ) is the stiffness coefficient,  $\sigma_1$  ( $N\ s\ m^{-1}$ ) is the damping coefficient, and  $\sigma_2$  ( $N\ s\ m^{-1}$ ) is the viscous friction coefficient, describing the Stribeck effect.  $\omega_S$ ,  $M_c$ ,  $M_S$  and  $\sigma_2$  are static friction parameters.  $\sigma_0$  and  $\sigma_1$  are dynamic friction parameters.

### 3.2 PSO-GA Algorithm Design

The PSO-GA algorithm, as a serial hybrid algorithm of PSO and GA algorithms, is proposed to complementary advantages of these two algorithms. The PSO-GA algorithm executes PSO algorithm first for generation  $I$  and the individuals with better fitness value than average population fitness value will serve as the next generation  $II1$ . The rest individuals will be evolved by GA algorithm to product the rest next generation  $II2$ . Then generation  $II1$  and generation  $II2$  will be grouped together as the next generation  $II$ , which will be regarded as the initial population for the next iteration of the PSO-GA algorithm. The above steps are repeated until the results satisfy certain conditions.

For LuGre friction model, there are six parameters  $\sigma_0$ ,  $\sigma_1$ ,  $\sigma_2$ ,  $\omega_S$ ,  $M_c$  and  $M_S$  to recognize, which can be as a parameter set for algorithm implementation. Each parameter in the set is preferentially distributed into a numerical interval to limit the PSO-GA algorithm search scope first to improve the operation efficiency.

The objective function (error indicator)  $J_m$  is selected as the evaluation index of the PSO-GA algorithm for LuGre friction model parameters identification, which is shown as Equation (5).

$$J_m = \sum_{i=1}^{N_{\text{PSO-GA}}} \frac{1}{2} (F_{\text{PSO-GA}i} - F_{\text{DOB}i})^T (F_{\text{PSO-GA}i} - F_{\text{DOB}i}), \quad m = 1, 2, \dots, N_{\text{PSO-GA}} \quad (5)$$

where  $F_{\text{PSO-GA}i}$  denotes the  $i$ -th friction estimated by PSO-GA algorithm, which represents the  $i$ -th friction

acquired by high-precision DOB being synchronous with  $F_{\text{PSO-GA}i}$ . To simplify the algorithm, let the population size (maximum of  $m$ ) be equal to the number of input particles  $N_{\text{PSO-GA}}$ .

Then set individual fitness function  $F(x_m)$  as per Equation (6).

$$\begin{cases} C_{\max} = \max\{J_m\} \\ F(x_m) = C_{\max} - J_m, \quad m = 1, 2, \dots, N_{\text{PSO-GA}}. \end{cases} \quad (6)$$

For PSO algorithm implementation, particle velocity  $V$  and position  $x$  can be updated according to Equations (7) and (8).

$$\begin{aligned} V_{ij}^{k+1} &= WV_{ij}^k + c_1 r_1 (p_{\text{best}ij}^k - x_{ij}^k) + c_2 r_2 (g_{\text{best}ij}^k - x_{ij}^k) \\ x_{ij}^{k+1} &= V_{ij}^{k+1} + x_{ij}^k, \\ i &= 1, 2, \dots, N_{\text{PSO}}; \\ j &= 1, 2, \dots, Q_{\text{srch}}; \\ k &= 1, 2, \dots, N_{\text{iterat}} \end{aligned} \quad (7)$$

$$\quad (8)$$

There are  $N_{\text{PSO}}$  particles in the swarm,  $Q_{\text{srch}}$ -dimension search space and  $N_{\text{iterat}}$  iteration cycles. In this paper,  $Q_{\text{srch}}$  equals six.  $W$  stands for the PSO inertia weight, which influences the particle global and local search ability.  $c_1$ ,  $c_2$ ,  $r_1$  and  $r_2$  are constants, which play an important regulating role in PSO implementation.  $c_1$  is the local learning factor, and  $c_2$  is global learning factor.  $r_1$  and  $r_2$  are random numbers uniformly distributed between 0 and 1.  $X_i = (x_{i1}, x_{i2}, \dots, x_{iQ_{\text{srch}}})$  and  $V_i = (v_{i1}, v_{i2}, \dots, v_{iQ_{\text{srch}}})$  represent the  $i$ -th particle position and speed respectively. The individual extremum  $p_{\text{best}ij}$  is the optimal position found by the  $i$ -th particle. The global extremum  $g_{\text{best}ij}$  is the optimal position the particle swarm have searched.

PSO-GA algorithm uses real number coding. The detailed implementation steps of PSO-GA algorithm are as follows:

Step 1: Initialize the population. Generate  $N_{\text{PSO-GA}}$  particles based on our experience, and set  $G_{\max}$  as the PSO-GA maximum generation. For PSO algorithm implementation part, set  $G_{\text{PSO}}$  as the PSO maximum generation,  $V_{\max}$  as maximum particle velocity and  $V_{\min}$  as minimum particle velocity. Initialize learning factor  $c_1$  and  $c_2$ . For GA implementation part, initialize the GA maximum generation  $G_{\text{GA}}$ , crossover probability  $P_c$  and mutation probability  $P_m$ .

Step 2: Calculate the fitness value of every individual particle according to Equation (5).

Step 3: Initialize the iteration count variable of the total PSO-GA loop  $M$ ,  $M = 1$ . Initialize the iteration count variable of the PSO loop  $N$ ,  $N = 1$ . Initialize the iteration count variable of the GA loop  $K$ ,  $K = 1$ .

Step 4: If  $M \leq G_{\max}$ , continue to the next step, otherwise go to step 14.

Step 5: Compare present individual particle fitness  $F(x_m)$  with the fitness of particles corresponding to  $p_{\text{best}}$  and  $g_{\text{best}}$  respectively to determine whether update the  $p_{\text{best}}$  and  $g_{\text{best}}$  by present individual particle.

Step 6: Update every particle velocity and position to generate next generation particles according to Equations (7) and (8).

Step 7: If  $N > G_{\text{ps0}}$ , or  $g_{\text{best}}$  value is good enough, go to the next step. Otherwise,  $N = N + 1$ , and jump to step 5.

Step 8: Sort  $N$  PSO-GA particles by fitness value, and choose the particles with larger fitness value than average fitness as the first part of the next generation  $Gen1_M$ . The rest particles will be as GA population to evolve.

Step 9: Do genetic manipulation, which includes reproduction operation, crossover operation and mutation operation successively.

Step 10: If  $K G_{\text{GA}}$ , jump to step 11. Otherwise,  $K = K + 1$ , and jump to step 9.

Step 11: Sort these particles by fitness value as the rest part of the next generation  $Gen2_M$ .

Step 12: Combine  $Gen1_M$  and  $Gen2_M$  into one part as the next generation  $Gen_{M+1}$ .

Step 13:  $M = M + 1$  and jump to step 4.

Step 14: Output the optimal solution, which includes the optimal fitness value and the corresponding particle.

There are no special demands for the working state of the servo platform in LuGre parameter identification process based on PSO-GA algorithm. The algorithm exhibits great robustness and adaptability.

#### 4 FRICTION COMPENSATION CONTROLLER DESIGN

The solution to TCS friction compensation is designed for engineering guidance, as (see Fig. 7).

The controller with friction compensation is designed as Figure 8 based on the scheme in Figure 7.

In Figure 8, *Switch1*, *Switch2* and *Switch3* are switches, which can be controlled by programming. The friction compensation controller is composed of two modules: the dotted area is mainly used to implement the friction torque measurement and the LuGre model parameters identification. When the dotted area works, *Switch1* and *Switch2* are in the connection state, and *Switch3* is in off state. The identified parameters are send to LuGre module by the dotted area. Then *Switch1* and *Switch2* are set in off state, and *Switch3* is in connection state to start the telescope ATP with friction torque compensation. Repeat above operations and choose optimal LuGre parameters to minimize the system error.

## 5 FRICTION COMPENSATION TECHNOLOGY VERIFICATION

To verify the feasibility of the friction compensation method proposed, engineering validation is required. The azimuth axis of a 1.2 m aperture optical telescope is chosen as the test subject.

### 5.1 The Controlled Plant Identification

The TCS affected by nonlinear disturbances is a kind of SISO (single-input single-output) system, which can be expressed mathematically via Equation (9).

$$\ddot{\theta} = f(\dot{\theta}, t) + bu(t) + d(t) \quad (9)$$

where  $\ddot{\theta}$  represents the TCS acceleration,  $f(\dot{\theta}, t)$  is the function of velocity  $\dot{\theta}$ ,  $u(t)$  is the TCS input, and  $d(t)$  is the friction suffered by TCS.

The telescope azimuth axis is studied as the controlled plant. Its frequency characteristics can be acquired by the frequency response analyzer, based on which we fit curves as shown in Figure 9.

Figure 9 shows the amplitude-frequency and phase-frequency characteristics of the azimuth axis respectively.

According to the fitting curves, azimuth axis transfer function can be simplified as per Equation (10).

$$G_p(s) \approx \frac{1}{0.0003s^2 + 0.1082s + 39.3918} \quad (10)$$

Azimuth axis is a second-order controlled plant, of which differential equation can be transformed by  $G_p(s)$  as per Equation (11).

$$\ddot{\theta} = -360.67\dot{\theta} - 131306\theta + 3333.33u \quad (11)$$

### 5.2 Friction Torque Measurement

The balancing moment method is chosen based on Newton's third law. The shafting friction torque and the traction force are equal and opposite, when motor works in balancing moment. Friction torques are measured by DOB combined with dynamometer on the platform as shown in Figures 10 and 11.

When the dynamometer measures and records the real friction torque, the corresponding friction torque observed by DOB in the controller is read. Then the contrastive analysis between the friction torque measured and the friction torque observed is carried on to test and correct the parameters of DOB. Through continuous calibration, DOB accuracy for friction torque observation can reach 96.94%, which is satisfactory to be applied for the LuGre model parameters identification, as shown in Figure 12.

To achieve ATP performance and friction torque characteristics of the azimuth axis at speed

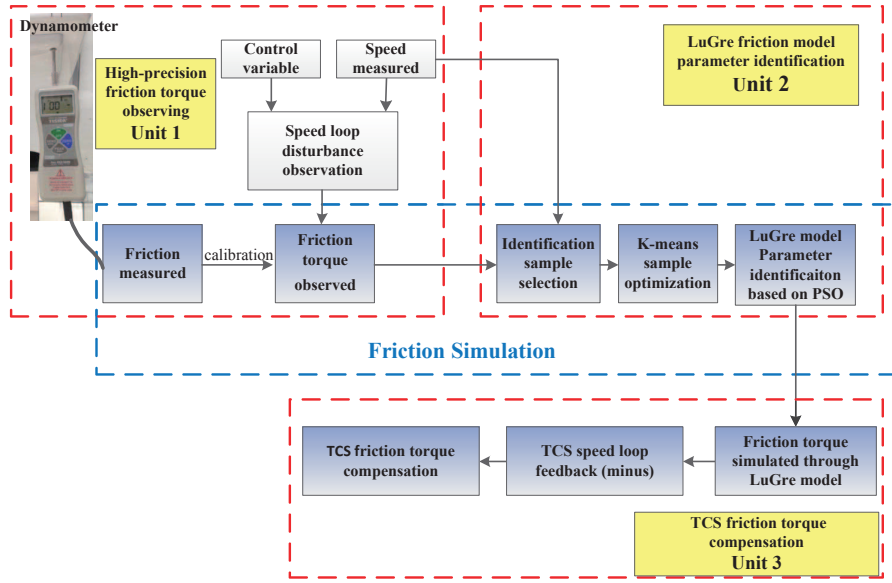


Fig. 7 The solution for TCS friction compensation.

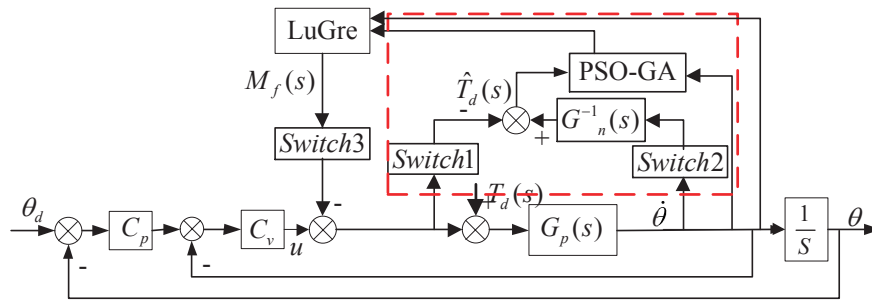


Fig. 8 The controller with friction compensation based on LuGre model.

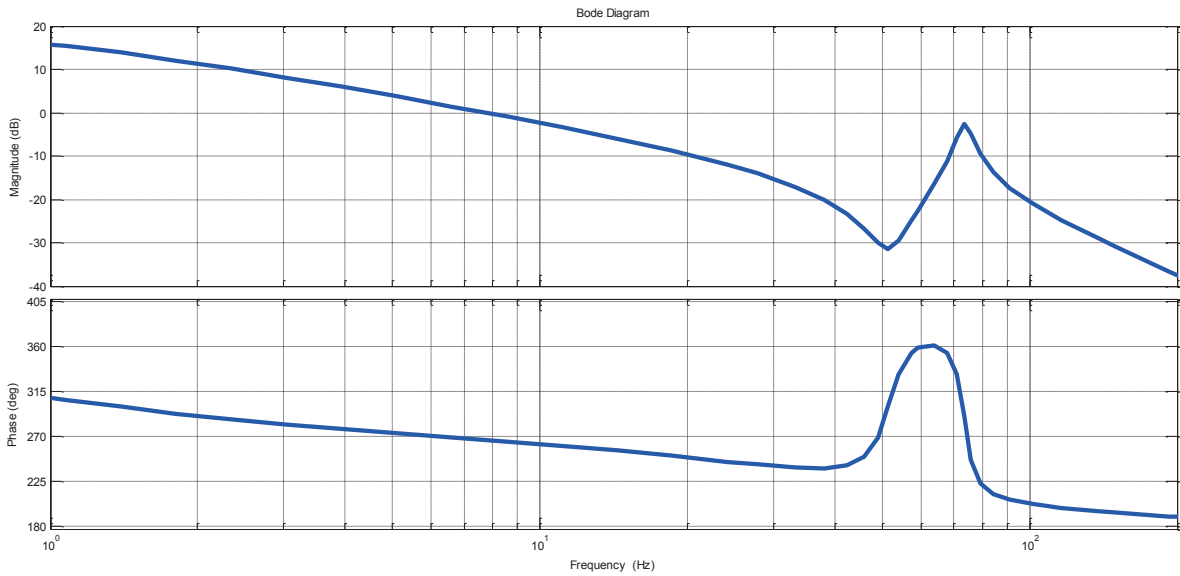


Fig. 9 Frequency characteristics fitting curves of telescope azimuth axis.



**Fig. 10** Telescope on-site debugging.



**Fig. 11** 1.2 m telescope out-field operation.

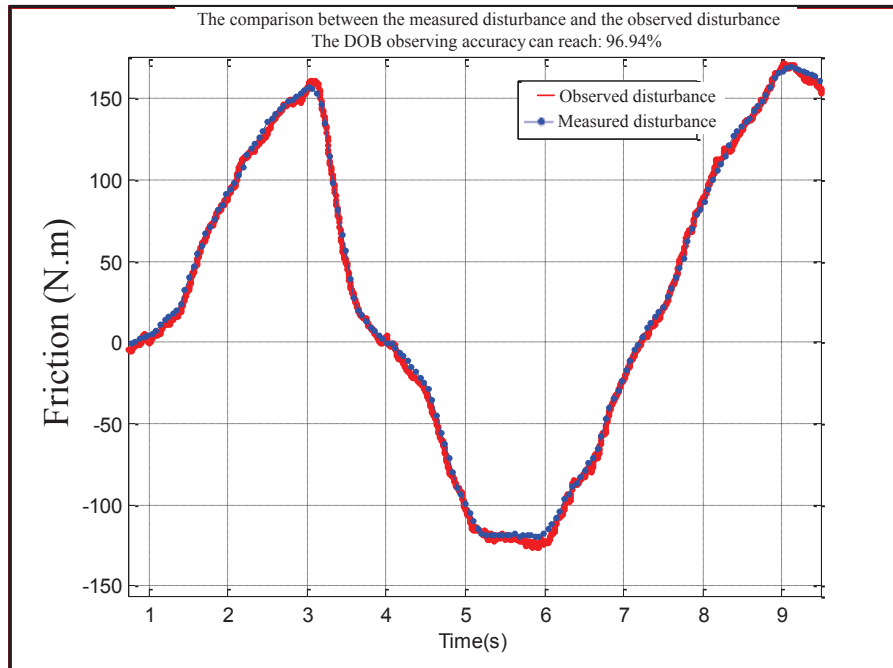


**Fig. 12** The friction observed after calibration vs. friction measured.

cross-zero working mode and low-speed working mode, 10 representative working speeds ( $1^\circ \text{ s}^{-1}$ ,  $0.1^\circ \text{ s}^{-1}$ ,  $0.0005^\circ \text{ s}^{-1}$ ,  $0.00025^\circ \text{ s}^{-1}$ ,  $0.0002^\circ \text{ s}^{-1}$ ,  $0.00019375^\circ \text{ s}^{-1}$ ,  $0.0001875^\circ \text{ s}^{-1}$ ,  $0.000175^\circ \text{ s}^{-1}$ ,  $0.00015^\circ \text{ s}^{-1}$  and  $0.0001^\circ \text{ s}^{-1}$ ) are selected as the leading speeds.

As an example, the performance of the azimuth at working speed  $0.1^\circ \text{ s}^{-1}$  is shown in Figure 13, and its corresponding friction torque observed is given in Figure 14.

The relationship between the friction torque and speed is shown in Figure 15, from which we can see that the

hysteresis is obvious. To ensure TCS tracking precision and speed stability, it is necessary to compensate for this friction torque.

### 5.3 The PSO-GA Friction Parameters Identification Experiment

The parameters identification is then performed based on PSO-GA.

Set the range of the LuGre friction model parameters estimated value  $\hat{H} = [\hat{\sigma}_0 \hat{\sigma}_1 \hat{\sigma}_2 \hat{M}_c \hat{M}_S \hat{\omega}_S]$  first. Assign the minimum solution value  $\text{Min}X = [4000 \ 9 \times$

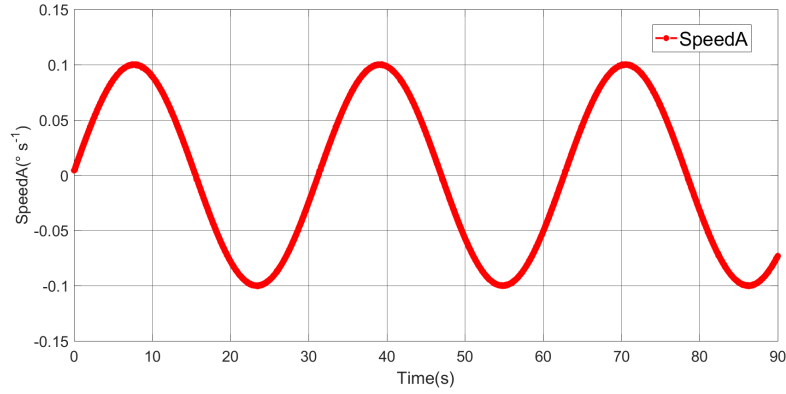


**Fig. 13** The performance of the azimuth at working speed  $0.1^\circ \text{ s}^{-1}$ .

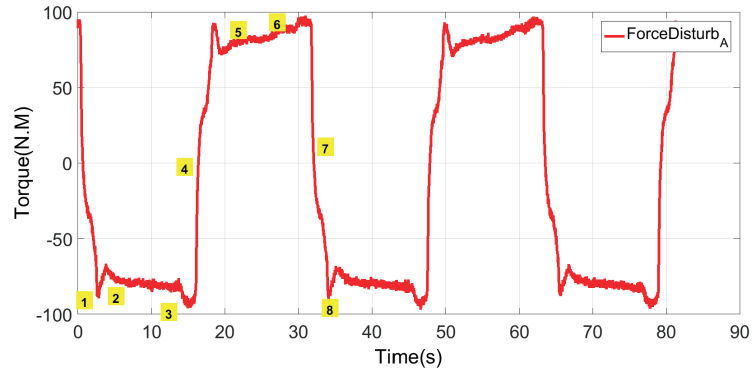


**Fig. 14** The friction torque measured of the azimuth at working speed  $0.1^\circ \text{ s}^{-1}$ .

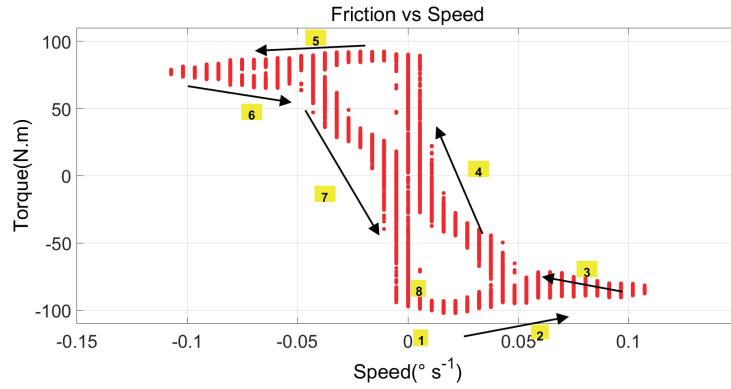


**Fig. 15** The relationship between friction torque and speed at working speed  $0.1^\circ \text{ s}^{-1}$ .

$10^5 \ 0 \ 50 \ 50 \ 0]$  and the maximum solution value  $\text{Max}X = [6000 \ 3 \times 10^6 \ 50 \ 100 \ 200 \ 1]$  by experience. Set iterative threshold value  $G_{\text{max}} = 300$ ,  $G_{\text{PSO}} = 300$ , and  $G_{\text{GA}} = 200$ . For PSO algorithm part, set the minimum value of particles flight velocity  $V_{\text{min}} = -1$  and the maximum value  $V_{\text{max}} = 1$ . Set the local learning factor  $c_1 = 1.3$  to be less than the global learning factor  $c_2 = 1.75$ . To make the identification process more rapidly and precisely, the LDW strategy (linear decreasing weight) is chosen, which

can be expressed as Equation (12).

$$W(i) = W_{\text{max}} - \frac{W_{\text{max}} - W_{\text{min}}}{G_{\text{PSO}}} \times i, \quad i = 1, 2, \dots, G_{\text{PSO}} \quad (12)$$

where  $W$  stands for the inertia weight,  $W_{\text{max}}$  represents the maximum weight and the  $W_{\text{min}}$  denotes the minimum value of the weight. Based on repeated experiments, we set an extreme value of  $W_{\text{max}} = 0.9$  and  $W_{\text{min}} = 0.1$ .

For GA algorithm part, proportion select method (roulette wheel selection method) is applied, which can be

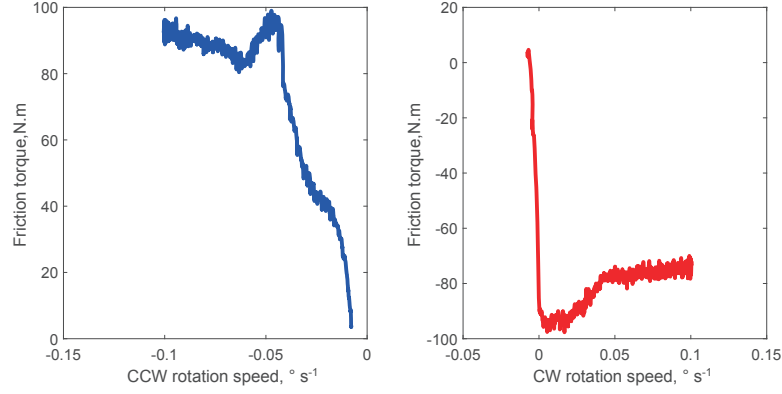


**Fig. 16** Friction torques of azimuth servo platform near the speed cross-zero. The left figure displays the friction torque of the azimuth servo turntable working in CCW direction near speed zero; The right figure shows the friction torque in CW direction.

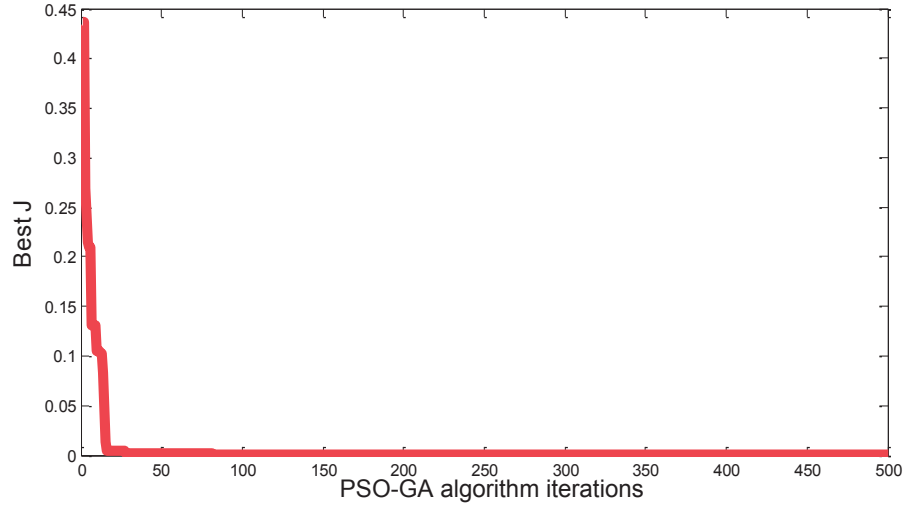


**Fig. 17** The best objective function value of each generation BestJ in the identification process.

**Table 2** The PSO-GA Parameter Identification Results

LuGre model parameters	CCW direction	CW direction	Unit
$\sigma_0$	$5.17 \times 10^3$	$5.15 \times 10^3$	N
$\sigma_1$	$10.12 \times 10^5$	$10.13 \times 10^5$	N s
$\sigma_2$	9.99	9.93	N s
$\omega_S$	0.035	0.033	$^\circ \text{s}^{-1}$
$M_c$	78.10	78.07	N m
$M_S$	117.17	117.11	N m

expressed by Equation (13) and Equation (14).

$$P(x_n) = \frac{F(x_n)}{\sum_{i=1}^{N_{GA}} F(x_i)}, \quad n = 1, 2, \dots, N_{GA} \quad (13)$$

$$q(n) = \sum_{j=1}^n P(x_j), \quad n = 1, 2, \dots, N_{GA} \quad (14)$$

where  $P(x_n)$  represents the probability of each individual passing on to the next generation and  $q(n)$  is the cumulative probability of each individual, which is

compared with a random number  $r$  between 0 and 1 to determine whether or not the particle  $x_n$  is selected into the next generation.

Here, crossover probability  $P_c = 0.9$  and mutation probability  $P_m$  are self-adaptive to improve the algorithm accuracy and accelerate the convergence speed, as shown in Equation (15).

$$P_m = 0.1 - \frac{0.01 \times i}{N_{GA}}, \quad i = 1, 2, \dots, N_{GA} \quad (15)$$

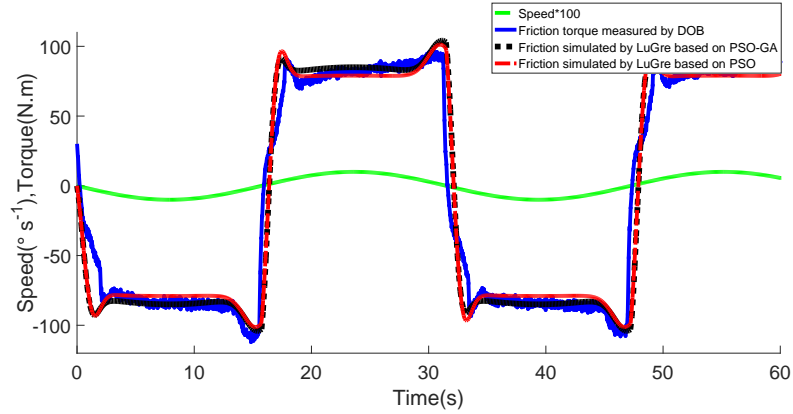


**Fig. 18** Comparison between the friction torque measured by DOB, friction simulated by LuGre based on PSO-GA and friction simulated by LuGre based on PSO.

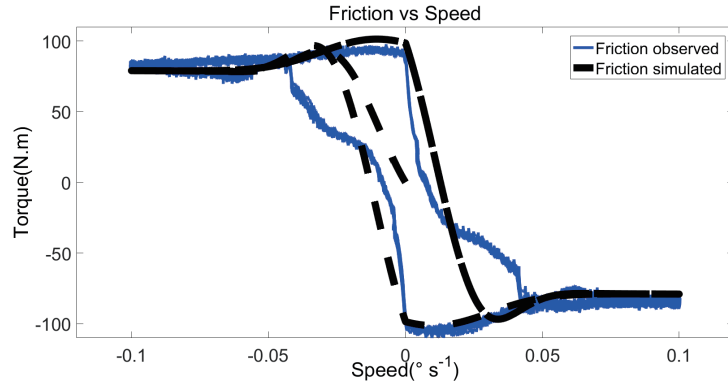


**Fig. 19** The friction-velocity observed vs. the friction-velocity simulated.

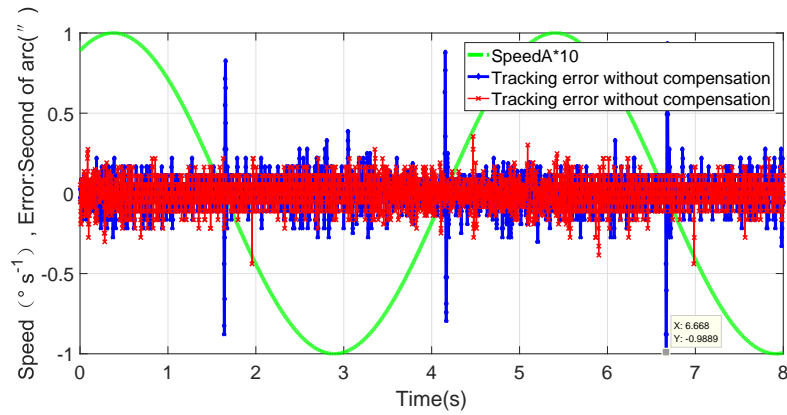


**Fig. 20** The azimuth performances at  $0.1^\circ \text{ s}^{-1}$  working mode before and after friction compensation.

4600 particles (Friction-Velocity points) are selected for each CCW (counterclockwise) direction and CW (clockwise) direction to be the LuGre model parameter identification particles of PSO-GA in TCS speed cross-zero operation, which are shown in Figure 16. The left figure displays the friction torque of the azimuth servo turntable working in CCW direction near speed zero, and the right figure shows the friction torque in CW direction, from which we can see the friction Stribeck effect clearly.

In the optimization process of LuGre model parameter identification, the minimum objective function ( $J_m$ ) of each generation BestJ is shown in Figure 17. Here BestJ can reach about  $4.033 \times 10^{-10}$ , which fully meets the identification accuracy requirements.

The LuGre parameters identified are shown in Table 2.

A comparison between the friction torque observed by DOB, friction simulated by LuGre model based on PSO-

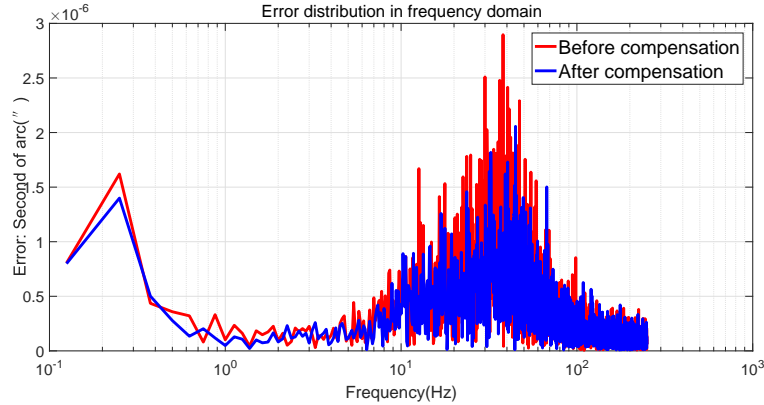


**Fig. 21** The azimuth performances in frequency domain at  $0.1^\circ \text{ s}^{-1}$  working mode before and after friction compensation.

**Table 3** The Azimuth Performance before and after Friction Compensation

Working Mode	Tracking error	Before compensation	After compensation
Speed cross-zero	Average positive peak	0.8926''	0.2252''
Speed cross-zero	Average negative peak	-0.3984''	-0.8881''
Tracking operation	Tracking error	0.1155''	0.0737''

GA algorithm and friction simulated by LuGre based on PSO algorithm only is given in Figure 18.

Compared with PSO algorithm applied in LuGre parameter identification, the PSO-GA algorithm owns a better identification ability when the friction suddenly changes and a closer amplitude recognition to the measured value when TCS works steadily. PSO algorithm needs 300 iterations more than PSO-GA to get this satisfactory result in this experiment. The RMSE (root-mean-square error) of the friction simulated by LuGre based on PSO only is about  $5.152N$ , while the RMSE of the friction simulated by LuGre based on PSO-GA is about  $2.573N$ .

In addition, a comparison between the friction-velocity observed by DOB and the friction-velocity simulated by LuGre based on PSO-GA algorithm is shown in Figure 19.

The friction simulated by LuGre based on PSO-GA agrees closely with the friction observed by DOB in speed cross-zero operation as well as at TCS steady working mode.

Through comprehensive analysis, a parameter identification method based on the PSO-GA algorithm for LuGre friction model is accurate and effective within the allowable range of error, which can be applied for TCS friction compensation.

## 5.4 The Experimental Results for Friction Compensation

Friction compensation for 1.2 m aperture telescope azimuth is performed according to the solution proposed in this paper. The performance of azimuth at a  $0.1^\circ \text{ s}^{-1}$  working mode is shown in Figure 20 and Figure 21. There is an overshoot error, which is opposite to the change direction of azimuth at speed cross-zero point, which hurts TCS stability badly. After the friction compensation, we can see that jitters at speed cross-zero point have been suppressed and the tracking error have been weakened obviously.

The engineering effectiveness of the method proposed in this paper is shown in Table 3.

When azimuth axis works at speed cross-zero work mode, the average positive peak to tracking error reduces from  $0.8926''$  to  $0.2252''$ , which is nearly 25.3% of the mean peak value without the compensation, and the absolute average negative peak to tracking error reduces from  $0.8881''$  to  $0.3984''$  after the friction compensation. The azimuth tracking error reduces from  $0.1155''$  to  $0.0737''$ , which decreases by 36.2% and meets the high precision and excellent stability requirements of TCS.

## 6 CONCLUSIONS

In this paper, a friction compensation method has been proposed based on high-precision LuGre parameters identification. To achieve high-precision friction torque first, we designed a DOB with dynamometer calibration. Then we propose a PSO-GA optimization algorithm for

LuGre friction model parameters identification, which combine their performance of both global searching ability and rapid convergence. The controller that integrates PID controller with DOB and friction compensation based on LuGre model is put forward for practical application to compensate for the TCS friction disturbance.

The friction compensation method proposed has been applied to a 1.2m aperture telescope for satellite-ground laser communication. The method has clearly proved to be effective, demonstrating strong reliability, favorable stability, and good real-time performance in an actual engineering application.

**Acknowledgements** This work was supported by the National Natural Science Foundation of China (NSFC) under Nos.11803017, 41904158, and 41774180, the China Postdoctoral Science Foundation under 2019M652385, the Open Research Program of the CAS Key Laboratory of Solar Activity under KLSA201907, and the National Astronomical Observatories and Young Scholars Program of Shandong University, Weihai (20820201005).

## References

- Brokate, M. 2000, Lectures on Applied Mathematics, 207
- Canudas de Wit, C., Olsson, H., Astrom, K., & Lischinsky, P. 1995, IEEE Transactions on Automatic Control, 40, 419
- Chen, Y., Han, B., Haitao, L. I., & Yang, L. 2012, Manned Spaceflight, 18, 62
- Dahl, P. R. 1976, AIAA Journal, 14, 1675
- Gajewski, J. B., & Glogowski, M. J. 2015, Tribology International, 87, 139
- Goubej, M., Popule, T., & Krejci, A. 2017, in Carpathian Control Conference, 93
- Guo, K., Pan, Y., & Yu, H. 2019, IEEE Transactions on Industrial Electronics, 66, 7841
- Haessig, David A., J., & Friedland, B. 1991, in Society of Photo-Optical Instrumentation Engineers (SPIE) Conference Series, 1482, Acquisition, Tracking, and Pointing V, eds. M. K. Masten & L. A. Stockum, 383
- Iskandar, M., & Wolf, S. 2019, in IEEE International Conference on Robotics and Automation ICRA, 7367
- Jiang, N., Jian, X., & Shu, Z. 2018, International Journal of Control Automation & Systems, 16, 1038
- Jorge, Y., Daniel, G. P., Vicente, D., & Oluremi, O. 2018, Sensors, 18, 490
- Ke, D., Cong, S., Kong, D. J., & Shen, H. 2019, IEEE Transactions on Industrial Electronics, 66, 358
- Kumar, T., & Banavar, R. 2011, Ifac Proceedings Volumes, 44, 980
- Kumar, T. S., & Banavar, R. N. 2018, Asian Journal of Control, 20, 678
- Le-Tien, L., & Albu-Schaffer, A. 2018, IEEE Transactions on Control Systems Technology, 26, 2259
- Li, X., Zhou, W., Luo, J., et al. 2019, IEEE Access, 7, 94400
- Lopes, R. A. M., Carrara, V., & Kuga, H. K. 2019, Computational & Applied Mathematics, 38, 1
- Puglisi, L. J., Saltaren, R. J., & Cena, C. E. G. 2017, Experimental Identification of Lu-Gre Friction Model in an Hydraulic Actuator, 13 (Springer, Cham), 133
- Qin, J., Léonard, F., & Abba, G. 2016, IEEE Transactions on Control Systems Technology, 24, 2207
- Rafan, N. A., Jamaludin, Z., & Heng, C. T. 2016, in 2016 International Conference on Computer and Communication Engineering (ICCCE), IEEE, 149
- Su, Y., Wang, Q., Yan, F., Liu, X., & Huang, Y. 2016, in Society of Photo-Optical Instrumentation Engineers (SPIE) Conference Series, 9682, 8th International Symposium on Advanced Optical Manufacturing and Testing Technologies: Large Mirrors and Telescopes, 96820C
- Sun, Y.-H., Sun, Y., Wu, C. Q., & Sepehri, N. 2018, International Journal of Control, 91, 770
- Tang, P., Xiao, S., & Li, Q. 2017, Bearing, 4, 5 (in Chinese)
- Wang, C.-J., Bai, J.-M., Fan, Y.-F., et al. 2019, RAA (Research in Astronomy and Astrophysics), 19, 149
- Wang, Q., Cai, H.-X., Huang, Y.-M., et al. 2016, RAA (Research in Astronomy and Astrophysics), 16, 124
- Wilhelm, F., Tamura, T., Fuchs, R., & Müllhaupt, P. 2016, IEEE Transactions on Control Systems Technology, 24, 1354
- Wu, W., Shang, J. Z., Cao, Y. J., & Yu, N. H. 2017, in International Conference on Material Engineering & Application, ICMEA2016, 730, Trans Tech Publ, 242
- Xie, X. 2010, Lubrication Engineering, 35, 27
- Yue, F., Li, X., Chen, C., & Tan, W. 2017, International Journal of Systems Science, 48, 374
- Zhou, W.-P., Zheng, Y., Guo, W., Yu, L., & Yang, C.-S. 2010, RAA (Research in Astronomy and Astrophysics), 10, 96